

Doped Mott insulators in the triangular-lattice Hubbard model

Zheng Zhu^{1,2}, D. N. Sheng³, and Ashvin Vishwanath¹

¹*Department of Physics, Harvard University, Cambridge, Massachusetts 02138, USA*

²*Kavli Institute for Theoretical Sciences, University of Chinese Academy of Sciences, Beijing 100190, China*

³*Department of Physics and Astronomy, California State University, Northridge, California 91330, USA*



(Received 30 November 2020; revised 23 March 2022; accepted 27 April 2022; published 10 May 2022)

We investigate the evolution of the Mott insulators in the triangular lattice Hubbard Model, as a function of hole doping δ in both the strong and intermediate coupling limits. Using the advanced density matrix renormalization group (DMRG) method, at light hole doping $\delta \lesssim 10\%$, we find a significant difference between strong and intermediate couplings. Notably, at intermediate coupling an unusual metallic state emerges, with short ranged spin correlations but long ranged spin-chirality order. Moreover, no clear Fermi surface or wave vector is observed, this chiral metal also exhibits staggered loop current, which breaks the translational symmetry. These features disappear on increasing interaction strength or on further doping. At strong coupling, the 120 degree magnetic order of the insulating magnet persists for light doping, and produces hole pockets with a well-defined Fermi surface. On further doping, $\delta \approx 10\% \sim 20\%$ SDW order and coherent hole Fermi pockets are found at both strong and intermediate couplings. At even higher doping $\delta \gtrsim 20\%$, the SDW order is suppressed and the spin-singlet Cooper pair correlations are simultaneously enhanced. We also briefly comment on the strong particle-hole asymmetry of the model.

DOI: [10.1103/PhysRevB.105.205110](https://doi.org/10.1103/PhysRevB.105.205110)

I. INTRODUCTION

A central issue in the physics of strongly correlated materials is the nature of the correlated phases that emerge on doping a Mott insulator. Given its relevance to the high-temperature cuprate superconductors, much effort have been devoted to doped Mott insulators in the square lattice Hubbard model [1–4]. However, the analogous problem on the triangular lattice is equally interesting and likely to exhibit new and distinct physics, due to magnetic frustration and the absence of nesting and particle-hole symmetry in the minimal models.

Experimentally, the discovery of the spin liquids [5,6] in organic materials [7–12] like κ -(BEDT-TTF)₂Cu₂(CN)₃, EtMe₃Sb[Pd(dmit)₂]₂ and κ -H₃(Cat-EDT-TTF)₂ has triggered substantial efforts on the triangular lattice Hubbard model, which is suggested to be the simplest model to understand unconventional correlated physics in these systems. More recently, the triangular lattice magnets including Ba₃CuSb₂O₉ [13], Yb₂Ti₂O₇ [14], Cs₂CuCl₄ [15,16], Ba₃CoSb₂O₉ [17], YbMgGaO₄ [18], TbInO₃ [19], NaYbO₂ [20,21], the transition-metal dichalcogenide (TMD) [22,23], as well as twisted bilayers of TMD [24–26] have been successively suggested to realize triangular lattice Hubbard models or their effective Heisenberg models. In a different background, the triangular Hubbard model was recently realized on optical lattices [27] with loading ultracold fermions [28–30]. In these platforms, both the coupling strength U/t and charge concentration are widely tunable and accurately controllable, which allow for probing the correlated electron physics on frustrated lattices.

Theoretically, the triangular lattice Hubbard model still poses a great challenge. At half filling, mean field approaches

[31–35] and numerical studies [36–58] have identified the metal-insulator transition (MIT) around $U_c/t \approx 5 \sim 8$, and two distinct Mott insulators: a 120° Néel ordered phase in the strong coupling $U \gg t$ limit, and a quantum disordered state, potentially a spin liquid phase, around the MIT. Away from half filling, the slave-boson mean field [59–62], renormalization group [63], and numerical calculations [64–69] have mainly focused on superconductivity and its pairing symmetry. Nevertheless, a systematic study of the correlated phases emerging from doped Mott insulators is a much-needed endeavor, where many open questions are of equivalent importance as the intensively investigated square lattice [2–4]. Motivated by the above, here we study the emergent correlated phases obtained on doping the distinct Mott insulators, which appear in the intermediate and strong coupling regimes, in the triangular lattice Hubbard model. We focus on hole doping the $t > 0$ model in Eq. (1) below.

II. MODEL AND METHOD

We consider the doped Hubbard model on a triangular lattice described by

$$H = -t \sum_{\langle i,j \rangle, \sigma} (c_{i\sigma}^\dagger c_{j\sigma} + \text{H.c.}) + U \sum_i n_{i\uparrow} n_{i\downarrow}, \quad (1)$$

where $\langle i, j \rangle$ denotes the nearest neighbor links, $c_{i\sigma}^\dagger$ ($c_{i\sigma}$) and $n_{i\sigma}$ represent the electron creation (annihilation) operators and number operators at site i with spin σ ($\sigma = \uparrow, \downarrow$), respectively, and we take $t > 0$; $U > 0$. We perform a comparative study of the doped Mott insulators with distinct emergent spin backgrounds [50,52–56]: (i) a quantum disordered spin

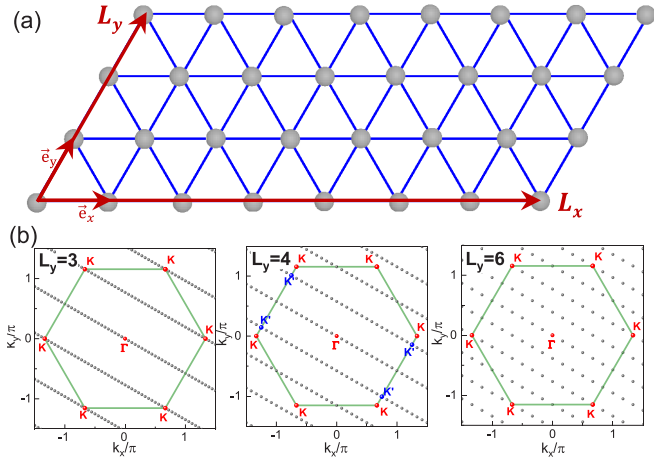


FIG. 1. Triangular lattice and the corresponding Brillouin zone. (a) The triangular lattice is spanned by the primitive vectors $\mathbf{e}_x = (1, 0)$ and $\mathbf{e}_y = (1/2, \sqrt{3}/2)$ with size $N = L_x \times L_y$. (b) The accessible momenta (black dots) in the first Brillouin zone and the high-symmetry points are shown in (b) for $L_y = 3$ (left), $L_y = 4$ (middle), and $L_y = 6$ (right) cylinders. The number of independent momenta equals to size N , panel (b) shows three examples: $L_x = 36$ (left), $L_x = 30$ (middle), and $L_x = 12$ (right).

background (“spin liquid”) that emerges at intermediate coupling strength and (ii) the magnetic ordered spin background with larger coupling strength. In this paper, we mainly focus on the hole doped side and identify the nature of various doping-induced phases. Considering the possible shift of the intermediate phase boundaries with system size [50,52–56], we choose different typical parameters of U/t for the doped magnetic disordered spin background and the doped magnetic ordered spin background.

Because of the lack of well-controlled theoretical methods in two-dimensional strongly correlated systems, quasi-one-dimensional systems have become a good starting point, allowing two-dimensional characteristics to emerge on growing the degrees of freedom compared to one dimension. More crucially, they allow performing accurate numerical density matrix renormalization group (DMRG) simulations, which have proved to be one of the most powerful numerical methods for strongly correlated systems such as the doped Mott insulators on the square lattice. Since the computational cost of DMRG [70,71] increases exponentially with system width, we focus on cylinders, similar to earlier DMRG studies on the square lattice. The cylinder is spanned by vectors $L_x \mathbf{e}_x = L_x(1, 0)$ and $L_y \mathbf{e}_y = L_y(1/2, \sqrt{3}/2)$ with circumference L_y , as illustrated in Fig. 1(a).

Figure 1(b) depicts the corresponding Brillouin zone for $L_y = 3, 4, 6$ cylinders, and the black dots represent the accessible momenta points on systems with size $N = L_x \times L_y$. Because of the fact that the spin long-range ordered phase becomes gapped for even L_y [72], it requires odd L_y and integral multiple of 3 for both L_x and L_y in order to capture the nature of the 120° Néel order. In particular, \mathbf{K} points are inaccessible on cylinders with $L_y = 4$, as shown in Fig. 1(b), we can only access \mathbf{K}' points, which are the closest momentum to \mathbf{K} . In the present paper, we mainly focus on $L_y = 3$ and

$L_y = 4$ in most cases, but also compare with $L_y = 6$ cylinders when identifying the wave vectors of the spin density waves (SDWs).

Depending on system size and physical quantity, the bond dimension is set up to $D = 45\,000$ when implementing $U(1) \times U(1)$ symmetry in the DMRG program, and up to $D = 23\,000$ when implementing $U(1) \times SU(2)$ symmetry [$\sim D = 69\,000$ in $U(1) \times U(1)$ program]. The cylinder length is pushed up to $L_x = 72$. We remark that the longer length also requires much larger bond dimension to get converged results for quantities such as the chiral correlations. For example, for the chiral-chiral correlations on $L_y = 4$ cylinders, we find that, at light doping, the converged measurement can only be obtained at $D = 23\,000$ with using $U(1) \times SU(2)$ symmetry, which roughly corresponds to $D \approx 69\,000$ when using $U(1) \times U(1)$ symmetry in the program. In particular, for the fast decay of the correlation functions, both power law and exponential function could fit the data well; to see it more clearly, we present both semilogarithmic and double-logarithmic plots for the same data to compare. To gain the indication of superconductivity for 2D, we look for power-law decay $r^{-\eta}$ with $\eta < 2$, which would lead to the divergence of superconductivity susceptibility.

III. RESULTS

A. Evolution of spin correlations with hole doping

We begin with probing the ground-state properties of the model Hamiltonian (1) as a function of hole doping δ in the spin channel by examining the spin structure factor

$$S_{\mathbf{q}}(\mathbf{Q}) = \frac{1}{N} \sum_{i,j} \langle S_i^z S_j^z \rangle e^{i\mathbf{Q} \cdot (\mathbf{r}_i - \mathbf{r}_j)}. \quad (2)$$

Here, we have confirmed that $\langle S_i^z \rangle$ is vanishingly small on each site. In our calculation, the hole doping is realized by removing equal number of spin-up and spin-down electrons, and we target the sector with total spin $S^z = 0$. Figures 2(a1)–2(a3), 2(b1)–2(b3), and 2(c1)–2(c3) show the contour plot of $S_{\mathbf{q}}$ at three typical hole doping concentrations for $U/t = 7.5$, $U/t = 9$, and $U/t = 18$, respectively. The spin structure factor for $U/t = 7.5$ and $U/t = 9$ exhibit similar behavior.

Spin correlations at intermediate coupling for $L_y = 3$. For $U/t = 7.5$ and $U/t = 9$, $S_{\mathbf{q}}$ are featureless at light doping [see Figs. 2(a1) and 2(b1) for $\delta = 1/18$], consistent with a spin disordered phase. With further doping, $S_{\mathbf{q}}$ exhibits sharp peaks at $\mathbf{Q} = \mathbf{K}$ for moderate doping [see Figs. 2(a2) and 2(b2) for $\delta = 1/6$], suggesting a doping induced commensurate SDW. The intermediate SDWs are finally suppressed on further increasing doping beyond 20% [see Figs. 2(a3) and 2(b3) for $\delta = 2/9$]. To probe the evolution of SDWs with hole doping, we keep track of $S_{\mathbf{q}}(\mathbf{K})$ as a function of δ , as shown in Figs. 2(a4) and 2(b4), $S_{\mathbf{q}}(\mathbf{K})$ is independent of L_x for $\delta \lesssim 10\%$ at intermediate coupling, consistent with a nonmagnetic spin background. However, on further increasing doping to $\delta \approx 10\% \sim 20\%$, $S_{\mathbf{q}}(\mathbf{K})$ is significantly enhanced, and its height also increases with system size, indicating the doping induced SDW, which finally disappears at $\delta \gtrsim 20\%$.

Spin correlations at strong coupling for $L_y = 3$. In contrast, on doping holes into the strong coupling $U/t = 18$ model,

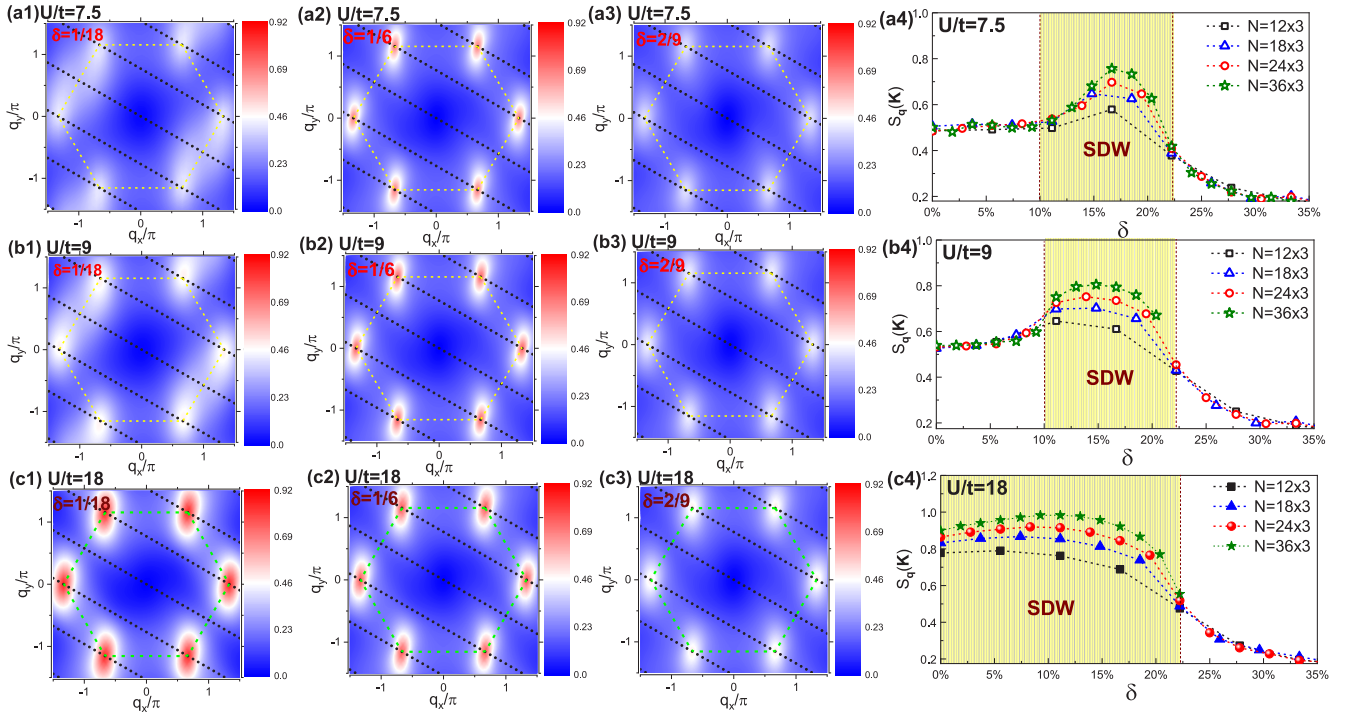


FIG. 2. The static spin structure factor $S_q(\mathbf{Q})$ as a function of hole doping concentration δ on $L_y = 3$ cylinders. Panels (a), (b), and (c) show the contour plot of $S_q(\mathbf{Q})$ for $U/t = 7.5$ [(a1)–(a4)], $U/t = 9$ [(b1)–(b4)], and $U/t = 18$ [(c1)–(c4)] with different δ . From left to right in each row, we consider three typical hole doping concentrations: $\delta = 1/18$ [(a1),(b1),(c1)], $\delta = 1/6$ [(a2),(b2),(c2)] and $\delta = 2/9$ [(a3),(b3),(c3)]. The black dots represent the accessible momenta in the Brillouin zone (dashed line) for $N = 24 \times 3$ cylinders, and the contour plot is created by using triangulation interpolation. Panels (a4), (b4), and (c4) show $S_q(\mathbf{Q})$ at $\mathbf{Q} = \mathbf{K}$ as a function of δ for $U/t = 7.5$, $U/t = 9$, and $U/t = 18$, respectively. The bond dimension of such calculation is set up to 6000~10 000.

a 120° Néel ordered spin background with sharp peaks in $S_q(\mathbf{K})$ survives until $\delta \approx 20\%$ for $L_y = 3$ [see Figs. 2(c1)–2(c3)]. Furthermore, the height of these peaks also increase with system sizes [see Fig. 2(c4)], indicating that the commensurate SDW order remains robust against hole doping in the strong coupling limit. At $\delta > 20\%$, the spin correlations become short ranged and are indistinguishable for all coupling strengths.

Spin correlations for $L_y = 4$. For wider cylinders with $L_y = 4$, we find the spin backgrounds at $\delta \lesssim 10\%$ also resemble the ones at half filling, as shown in Figs. 3(a) and 3(d). Although the momenta \mathbf{K} are inaccessible for $L_y = 4$ and the spin ordered phase becomes spin gapped due to the even-leg effect, the intensity of S_q is concentrated at the momentum closest to \mathbf{K} (i.e., \mathbf{K}') in the strong coupling limit (at $\delta \lesssim 10\%$). These facts indicate the nature of spin background at light doping is mainly determined by coupling strength U/t . At moderate doping $\delta \approx 10\% \sim 20\%$, the commensurate SDWs exhibits competing wave vector \mathbf{M} , as shown in Figs. 3(b) and 3(e). To show it more clearly, we study S_q at \mathbf{M} and in the vicinity of \mathbf{K} as a function of hole doping, as shown in Figs. 3(a) and 3(d), the intensity of $S_q(\mathbf{M})$ is enhanced at moderate doping, while the SDWs are finally suppressed for larger doping $\delta \gtrsim 20\%$.

We also notice the competing wave vectors of the SDW, which is determined by the coupling strength U/t . The SDW with wave vector $\mathbf{Q} = \mathbf{M}$ is dominant at moderate coupling strength, however, with the increase of coupling strength U/t , the SDW with $\mathbf{Q} = \mathbf{K}'$ becomes competitive, as indicated

from Figs. 3(a) and 3(d). We also have checked the $t - J$ model, which corresponds to the effective Hamiltonian of Hubbard model in the $U/t \rightarrow \infty$ limit, and confirmed that the dominant wave vector of SDW is $\mathbf{Q} = \mathbf{K}'$ in the strong coupling limit. Such competition might be induced by the special feature of $L_y = 4$ cylinders, where \mathbf{K} points are inaccessible. To further confirm it, we also check $L_y = 6$ cylinders and find that when both the momenta \mathbf{K} and \mathbf{M} are accessible, the commensurate SDW with wave vector $\mathbf{Q} = \mathbf{K}$ is dominant at these dopings, as shown in Figs. 3(c) and 3(f).

B. Evolution of spin chirality with hole doping

To further investigate the nature of magnetic disordered spin background at $\delta \lesssim 10\%$ with intermediate coupling strength, we examine the spin chiral order by computing the chiral-chiral correlations $|\langle C_{\Delta_i} C_{\Delta_{i+r}} \rangle|$, where the chiral operator $C_{\Delta_i} = \mathbf{S}_{i_1} \cdot (\mathbf{S}_{i_2} \times \mathbf{S}_{i_3})$ is defined on the triangle formed by three nearest neighboring sites i_1 , i_2 , and i_3 . As shown in Fig. 4(a) for $L_y = 3$ cylinders and Fig. 4(b) for $L_y = 4$ cylinders at three typical hole doping concentrations: $\delta = 1/18$, $\delta = 1/6$, and $\delta = 1/3$.

At light doping $\delta \lesssim 10\%$, the chiral correlations decay much slower than r^{-1} [see the orange line in Fig. 4(a)] for $L_y = 3$ at $U/t = 7.5$ and slightly slower than r^{-2} [see the red line in Fig. 4(b)] for $L_y = 4$ at $U/t = 9$. The blue lines in Figs. 4(a) and 4(b) follow the amplitude of the chiral correlations, which can directly compare with the decay rate r^{-1} (orange line) and r^{-2} (red line), respectively. These results

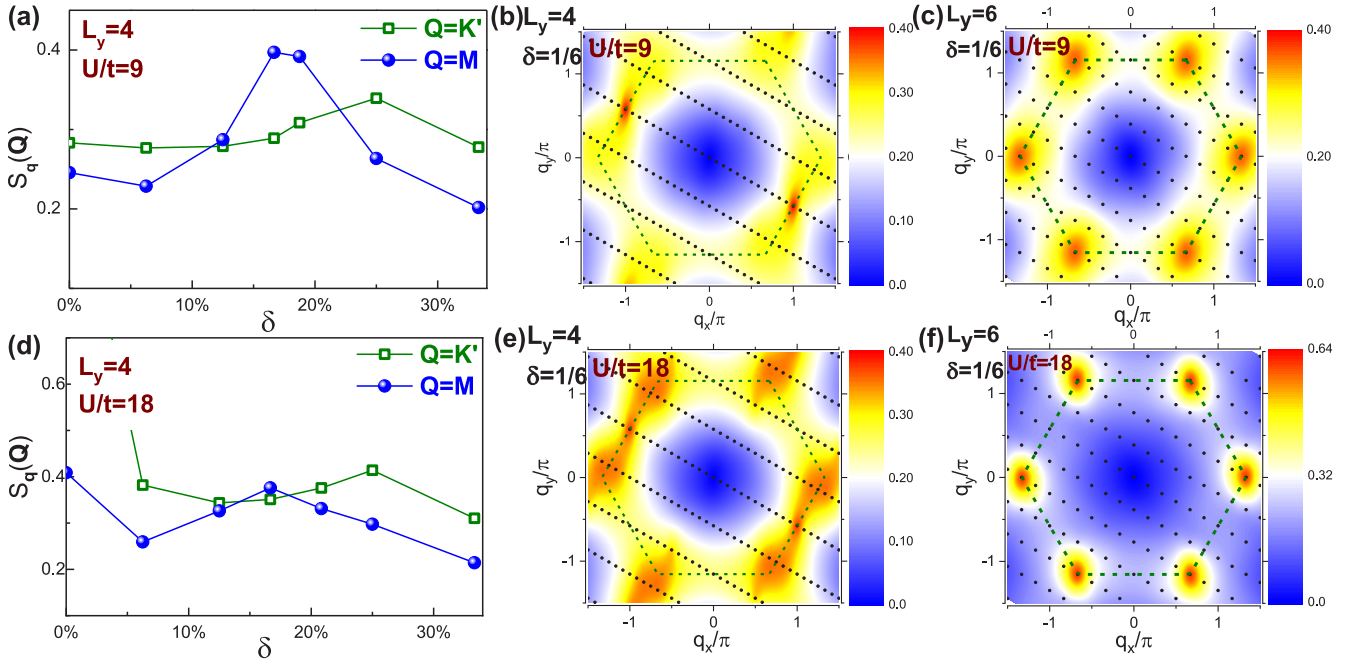


FIG. 3. The static spin structure factor $S_q(\mathbf{Q})$ on $L_y = 4$ and $L_y = 6$ cylinders. Panel (a) and (d) show S_q as a function of hole doping δ for $U/t = 9$ and $U/t = 18$ at momentum \mathbf{M} and \mathbf{K}' on $N = 24 \times 4$ cylinders. Panel (b) and (e) show the contour plot of $S_q(\mathbf{Q})$ for $U/t = 9$ (b) and $U/t = 18$ (e) with $\delta = 1/6$ and $N = 24 \times 4$. Panel (c) and (f) show the similar plot of $S_q(\mathbf{Q})$ to (b) and (e) but on $L_y = 6$ cylinders with $L_x = 12$. The black dots represent the accessible momenta points in the Brillouin zone (dashed line) and the contour plot is created by using triangulation interpolation. The bond dimension of these calculations is set up to 30 000~35 000.

suggest the (quasi-)long range chiral order at light doping. We also check $U/t = 9$ for $L_y = 3$ and $U/t = 10$ for $L_y = 4$, as shown in Fig. 4(c), which exhibit similar quasi-long-range chiral correlations decaying in a power-law fashion. Here we point out that $U/t = 9$ and $U/t = 10$ are similar for $L_y = 4$, while the chiral correlations at $U/t = 9$ decay faster than $U/t = 7.5$ but comparable to r^{-2} , which indicates the increase of the coupling strength U/t would suppress the chiral correlations, but the spin background is still nonmagnetic according to the featureless spin structure factor S_q in Fig. 2(a1). When we increase the doping to $\delta \gtrsim 10\%$, the chiral correlations are strongly suppressed and decay faster than r^{-2} , as shown in Figs. 4(a) and 4(b).

We also point out that the chiral correlations have sign fluctuations for $L_y = 3$ but not for $L_y = 4$ for half filling, consistent with Refs. [53,54], however, at light doping, both cases exhibit the change of sign with distance r . In particular, we notice that, the claim of absence of chiral spin liquid at half-filling for $L_y = 3$ in Ref. [73] also conflicts with other DMRG studies [53,54,74].

C. SDW vs CDW

For the doped Mott insulators on square lattice, the doped charge would suppress the Néel order at light doping, and the CDW, such as the unidirectional stripes, would emerge around $\delta \approx 1/8$. Here, on the triangular lattice, from the above results of the spin structure factor $S_q(\mathbf{Q})$ and the chiral-chiral correlations $|\langle C_{\Delta_i} C_{\Delta_j} \rangle|$, we find the nature of the spin background is robust against hole doping and also find the robust spin density

waves at moderate doping $\delta \approx 10\% \sim 20\%$. In this section, we directly compare the spin-spin correlations $|\langle S_i^z S_{i+r}^z \rangle|$ with the charge density-density correlations $|\langle n_i n_{i+r} \rangle - \langle n_i \rangle \langle n_{i+r} \rangle|$ to examine the dominant correlations.

At light doping $\delta \lesssim 10\%$, as shown in Figs. 5(a) and 5(b), the spin-spin correlations decay slightly slower than the charge density-density correlations or with comparable rate, the amplitude of the spin-spin correlations is also larger. The red lines in Figs. 5 represent the decay rate $\sim r^{-2}$, which can be used for guidance. With increasing the hole doping to moderate level $\delta \approx 10\% \sim 20\%$. The charge density-density correlations are almost unchanged or slightly suppressed [see Figs. 5(a) and 5(b)]; however, the spin-spin correlations are significantly enhanced with both much slower decay rate and larger amplitude. The orange lines in Figs. 5 suggest the decay rate of the spin-spin correlations close to $\sim r^{-1.5}$ for $L_y = 3$ and is further enhanced to $\sim r^{-0.8}$ for wider cylinders $L_y = 4$. Since the power-law decay $\sim r^{-\alpha}$ with $\alpha < 2$ suggests the diverged susceptibility towards 2D, these observations indicate that the SDW would be dominant over the CDW for the doped Mott insulators on the triangular lattice.

Here we point out that a recent paper [73] also shows similar findings, i.e., the comparable decay rate of both correlations and the larger amplitude of the spin correlations. Although both correlators can be fitted by the power-law function with close exponents similar to our findings in Figs. 5(a) and 5(b), their interpretations that the spin correlations are exponentially decaying while the charge density correlations are power law in Ref. [73] are inconsistent with our results.

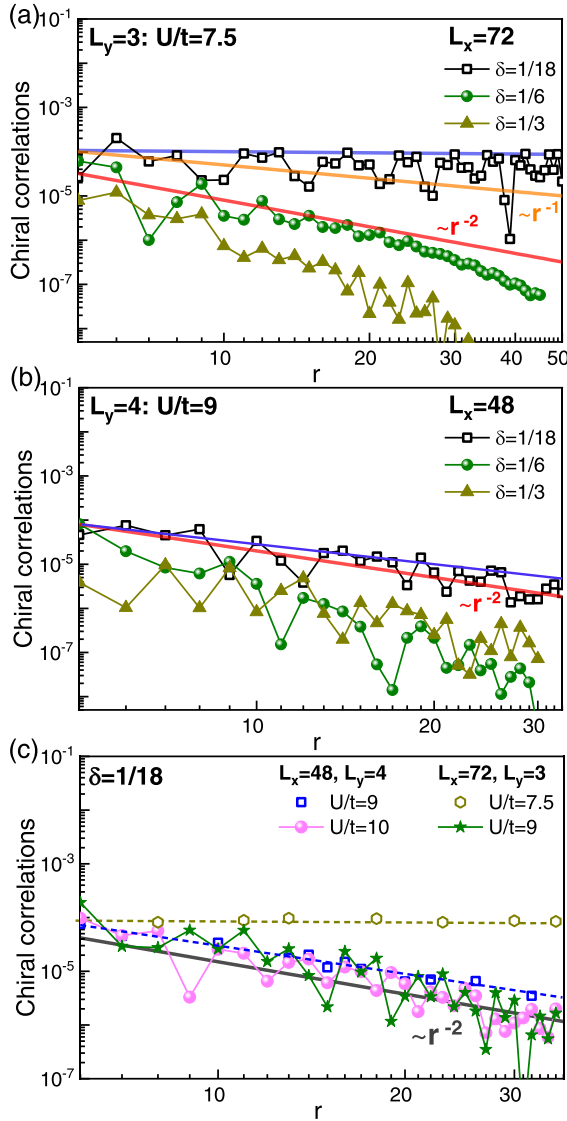


FIG. 4. Chirality correlators. The chiral-chiral correlations as a function of distance r for three typical hole doping at $U/t = 7.5$ on $N = 72 \times 3$ cylinders (a) and at $U/t = 9$ on $N = 48 \times 4$ cylinders (b). The solid lines represent the power-law function of r^{-2} (red) and r^{-1} (orange). The blue-solid lines correspond to the decay of chiral correlations. The bond dimension of such calculation is set up to 36 000~60 000 for $L_y = 3$ in (a) and up to 36 000~69 000 for $L_y = 4$ in (b). Panel (c) shows additional results at $U/t = 9$ on $N = 72 \times 3$ cylinders and at $U/t = 10$ on $N = 48 \times 4$ cylinders, we also include the results (a) and (b) to compare.

D. Hole pockets evolution with doping

In the charge channel, we examine the properties of doped holes by measuring the hole momentum distribution $n^h(\mathbf{k})$, which can be extracted from the change of electron momentum distribution after doping:

$$n^h(\mathbf{k}) \equiv n_0(\mathbf{k}) - n_\delta(\mathbf{k}), \quad (3)$$

where

$$n_\delta(\mathbf{k}) = \frac{1}{N} \sum_{i,j,\sigma} \langle c_{i\sigma}^\dagger c_{j\sigma} \rangle e^{i\mathbf{k} \cdot (\mathbf{r}_i - \mathbf{r}_j)} \quad (4)$$

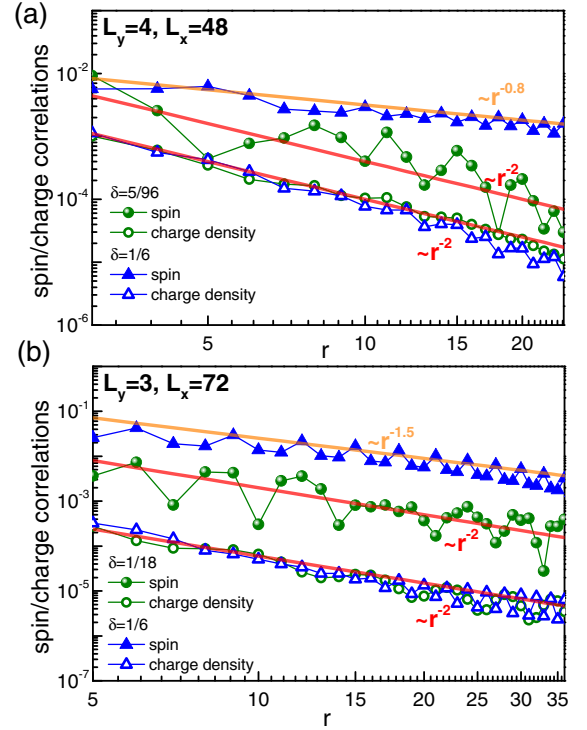


FIG. 5. Spin-spin correlations and charge density-density correlations. Panels (a) and (b) show the comparison between the spin-spin correlations and charge density-density correlations for $U/t = 9$ on $L_y = 4, L_x = 48$ and $L_y = 3, L_x = 72$ cylinders. We consider two typical examples at light doping and moderate doping. Both correlations decay in a comparable rate at light doping, however, at moderate doping, the spin-spin correlations decay much slower than the charge density-density correlations and also with much larger amplitude. The bond dimension of such calculation is set up to 60 000 for light doping and up to 36 000 for moderate doping $\delta \lesssim 10\%$.

represents the electron momentum distribution at hole doping δ , $n_0(\mathbf{k})$ corresponds to half filling at the same coupling strength U/t .

At light hole doping $\delta < 10\%$, we find the following contrasting outcomes depending on whether one is at strong or intermediate coupling. At strong coupling, the doped holes form small pockets around momenta \mathbf{K} [see Fig. 6(c) for $U/t = 18$], while at intermediate coupling each hole pocket splits into two parts [see Fig. 6(a) for $U/t = 9$]. To see this more clearly, we show the cuts of $n^h(\mathbf{k})$ across the hole pockets in Fig. 6(e). Strikingly, at strong coupling there is a sharp drop in $n^h(\mathbf{k})$ characterizing a well-defined Fermi momentum of holes in the spin ordered background, while at intermediate coupling there is a broad momentum distribution for lightly doped holes. The latter is indicative of fractionalized spin and charge excitations—although the total momentum of the spin and charge is conserved [75,76], the momentum shared between separated charge and spin excitations would lead to the absence of a well-defined Fermi momentum for holes [75–80]. Here we also point out that the splitting of hole pockets at intermediate coupling is independent of L_x , and gradually disappears with increasing coupling strength

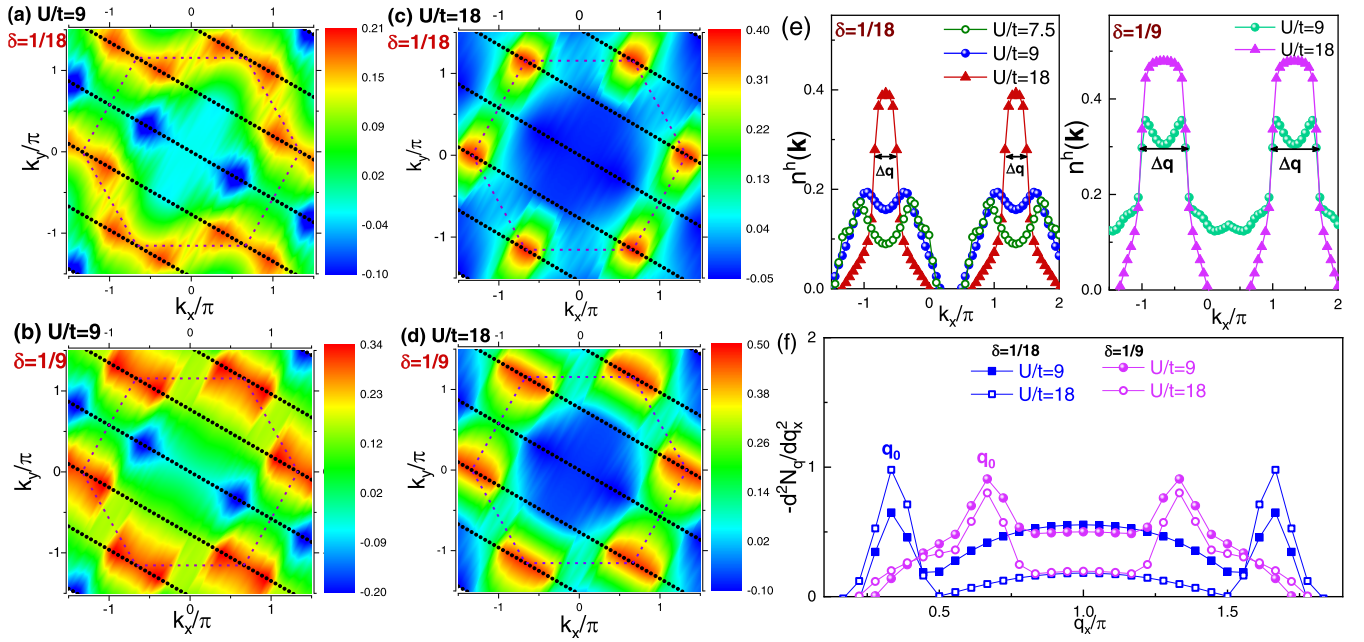


FIG. 6. The properties of doped holes in Fermi surface and charge structure factor. [(a)–(d)] The contour plot of electron momentum distribution $n^h(\mathbf{k})$ for $U/t = 9$ [(a),(b)] and $U/t = 18$ [(c),(d)] at doping $\delta = 1/18$ and $\delta = 1/9$. The black dots represent the accessible momenta points in the Brillouin zone, and the contour plot is created by using triangulation interpolation. Panel (e) shows the cuts of $n^h(\mathbf{k})$ through \mathbf{K} at doping $\delta = 1/18$ (left) and $\delta = 1/9$ (right), respectively. Panel (f) shows the second order derivatives of the density structure factor N_q , the peaks at q_0 indicate the wave vector of charge modulations. Here we consider $N = 36 \times 3$ cylinders. The bond dimension of such calculation is set up to 10 000–12 000.

to the strong coupling regime, as shown in the left panel in Fig. 6(e).

E. Chiral metallic phase

We further compared $n^h(\mathbf{k})$ with charge density structure factor N_q . N_q is defined by the Fourier transformation of density-density correlations, i.e.,

$$N_q = \frac{1}{N} \sum_{i,j} (\langle n_i n_j \rangle - \langle n_i \rangle \langle n_j \rangle) e^{i\mathbf{q} \cdot (\mathbf{r}_i - \mathbf{r}_j)}. \quad (5)$$

As shown in Fig. 6(f), the peaks in the second order derivative of N_q characterize wave vectors of the charge modulations \mathbf{q}_0 , or equivalently, the scattering between holes near the Fermi surface with momentum difference $\Delta\mathbf{q}$. For a Fermi liquid state that appears to be present in the strong coupling regime, $\mathbf{q}_0 = \Delta\mathbf{q}$, where the corresponding charge modulations (see Appendix A 1) can be attributed to the intra-pocket scattering.

A striking observation is that in the anomalous chiral metal (the lightly doped intermediate coupling state) we find charge modulations with the *same* wave vectors \mathbf{q}_0 as in the strong coupling limit. However, unlike in the strong coupling limit, a well-defined Fermi momentum for doped holes is lacking [see Fig. 6(e)]. The significant difference between N_q and $n^h(\mathbf{k})$ suggests the spin and charge are no longer confined together in the anomalous chiral metal, consistent with doping a spin liquid. At larger doping $\delta \gtrsim 10\%$, a well-defined hole pocket is reconstructed even at intermediate coupling strength around \mathbf{K} [see Fig. 6(b)], while for the strong coupling strength, the original hole pockets gradually increase with doping [see

Fig. 6(d)]. Both cases have the same Fermi momentum, as illustrated by the jump in $n^h(\mathbf{k})$ in Fig. 6(e). The momentum difference $\Delta\mathbf{q}$ between holes near the Fermi surface exactly matches the peak \mathbf{q}_0 in the second-order derivative of the charge structure factor N_q , i.e., $\mathbf{q}_0 = \Delta\mathbf{q}$.

Moreover, we compare various real-space correlators to further examine the chiral metallic phase. As shown in Fig. 7(a) for $L_y = 4$ cylinders, we find the single particle propagator decays in a power-law fashion with a slower decay rate compared with other correlations, suggesting the robust nature of chiral metallic phase on $L_y = 4$ cylinders. However, we also point out that we find a complex feature on $L_y = 3$ cylinders [see Fig. 7(b)]: (i) the spin chirality order is dominant over other correlations for long distance on $L_y = 3$ cylinders, indicating a robust time-reversal symmetry breaking phase; (ii) the single particle propagator decays relatively faster than $L_y = 4$ but tends to saturate at longer distance and decays comparable with chiral correlations; and (iii) the spin-spin correlations ($\sim r^{-2.8}$) decay in a comparable rate with the pair-pair correlations [see the next section and Fig. 9(b)] and exhibiting spatial oscillations, which suggests the pair-density-wave (PDW) pattern is locally robust but the quasi-long-range order is insignificant. Therefore, the $L_y = 3$ cylinder exhibits the competition between the chiral metal and local PDW.

We further probe the nature of this chiral metal state by examining the bond charge current pattern, which is defined by $I_{(ij)}^c \equiv -i \sum_{\sigma} \langle c_{i\sigma}^\dagger c_{j\sigma} - \text{H.c.} \rangle$. A typical example of the current pattern at $\delta = 1/20$ for $U/t = 9$ is shown in Fig. 8, where the width of each bond is proportional to the

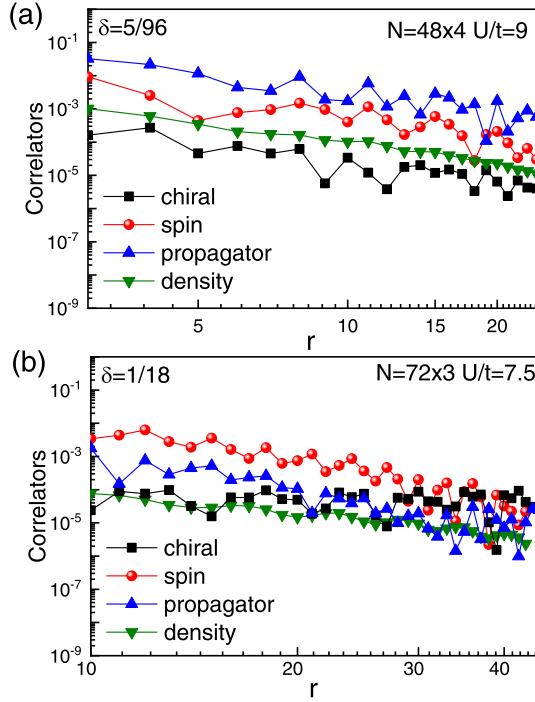


FIG. 7. Real-space correlators at light doping: chiral-chiral correlations, spin-spin correlations, charge density-density correlations, single particle propagators. Panel (a) and (b) show different correlators for $U/t = 9$ on $L_y = 4$ and for $U/t = 7.5$ on $L_y = 3$ cylinders, respectively. Here we focus on the doping.

current magnitude and the arrow indicates the current direction, the bond current pattern exhibits the translational symmetry breaking in the bulk along the horizontal direction, though we also notice the existence of domains in the pattern. We find $L_y = 3$ cylinders exhibit the same feature with $L_y = 4$, and leave such results in the Appendix A 2. Meanwhile, the time-reversal invariant spin current $I_{ij}^s \equiv -i\langle S_i^+ S_j^- - S_i^- S_j^+ \rangle$ [76] is vanishingly small in the same phase, consistent with the existence of the spin chirality order for chiral metal. Here, we would like to mention that the chiral metal phase identified here is consistent with recent mean-field analysis of the doped Kalmeyer-Laughlin type chiral spin liquid [81], where a chiral metal with unit cell doubling and staggered loop current order is proposed [82]. Reference [82] also points out the competition between the chiral metal and superconductivity, which is also observed here for $L_y = 3$. But with the increase of cylinder width, we find the chiral metallic phase becomes dominant.

F. Evolution of superconducting pair-pair correlations with hole doping

Below we examine the superconductivity on hole doping by measuring the pair-pair correlations $D(r) \equiv \langle (\hat{\Delta}_i^{s,t})^\dagger \hat{\Delta}_{i+r}^{s,t} \rangle$, in which the Cooper pair operators in the singlet and triplet channels are defined by $\hat{\Delta}_i^s \equiv \frac{1}{\sqrt{2}} \sum_{\sigma} \sigma c_{i, \sigma} c_{i, -\sigma}$, and $\hat{\Delta}_i^t \equiv \frac{1}{\sqrt{2}} \sum_{\sigma} c_{i, \sigma} c_{i, -\sigma}$, respectively. Here, we focus on the local pairing between the nearest sites (i_1, i_2) . We have fixed one bond in the pair-pair correlations at i along \mathbf{e}_y and measure its

correlations with pairs along \mathbf{e}_y , \mathbf{e}_x , and $\mathbf{e}_x - \mathbf{e}_y$, respectively, then we average the absolute value of pair correlations for a fixed distance. Figures 9(a) and 9(b) show the pair-pair correlations for $U/t = 7.5, 9$ for $L_y = 3$ and $U/t = 9$ for $L_y = 4$ at typical doping levels on $L_y = 3, 4$ cylinders, and $U/t = 18$ gives similar results. For both intermediate coupling and strong coupling models, we find the pairing strength in singlet channel are stronger than triplet channel, and thus we will focus on singlet pairing. We also notice that, at larger doping $\delta > 20\%$, while the singlet pairing has stronger correlations at longer distance, the triplet pairing becomes competitive with singlet pairing when further increasing δ , particularly for wider systems.

In our quasi-one-dimensional setup, true long-range order in the pair correlation function $D(r)$ is forbidden by the Mermin-Wagner theorem. We therefore content ourselves with looking for slow power-law decay [$D(r) \sim 1/r^\eta$ where $\eta \sim 1$], which, as we show, appears at the largest cylinder circumferences and at high doping. To gain the indication of superconductivity for 2D, we look for power-law decay with $\eta < 2$, which would lead to the divergence of superconductivity susceptibility. For the fast decay of the correlation functions, both power law and exponential function could fit the data well, to see it more clearly, we present both semilogarithmic and double-logarithmic plot for the same data to compare, as shown in Fig. 9.

For $L_y = 4$ cylinders, as shown in Fig. 9(a), the pair-pair correlations $D(r)$ decay exponentially at light doping, while its amplitude and decay length increase with the increase of hole doping. At moderate hole doping $\delta \approx 10\% \sim 20\%$, $D(r)$ could be fitted by an exponential function with long decay length or a power-law function with relatively large exponent $\eta \gtrsim 2$, as shown in the semilogarithmic and double-logarithmic plot in Fig. 9(a). Due to the large exponent, the power-law fitting and the exponential fitting would be very close, implying that the superconductivity is not dominant when the SDWs exist. At $\delta \gtrsim 20\%$, the pair-pair correlations are further enhanced when the SDWs are suppressed. The double-logarithmic in the right panel of Fig. 9(a) shows $\eta \approx 1.6$ at $\delta = 1/3$. Here, we push our calculation with bond dimension up to 60 000 and also plot the r^{-2} decay for comparison, we find that the power-law decaying behavior with exponent $\eta < 2$ is robust at large doping. The last observation gives evidence for quasi-long-range pair-pair correlations being stabilized at these relatively large dopings. Although the short-ranged spin backgrounds appear on wider cylinders already at $\delta \sim 20\%$, pushing to higher dopings considerably strengthens the pair-pair correlations.

For $L_y = 3$ cylinders, as shown in Fig. 9(b), the pair-pair correlations $D(r)$ decay rapidly at light doping $\delta = 1/18$. As shown in the semilogarithmic plot in Fig. 9(b), $D(r)$ could be fitted by an exponential function, meanwhile, it is potentially also consistent with a power law $D(r) \sim 1/r^\eta$ with large exponent $\eta \sim 3.7$ for $U/t = 9$ and $\eta \sim 2.8$ for $U/t = 7.5$, see the double-logarithmic plot in Fig. 9(b). Both fitting are quite close due to the smallness of correlators both in absolute magnitude and rapid decay rate, which does not point to a robust superconducting ground state, particularly considering that $\eta > 2$ corresponds to the short-ranged correlations in 2D or the superconducting susceptibility does not diverge.

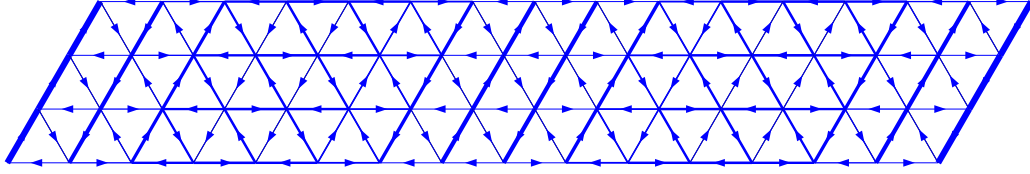


FIG. 8. The charge current pattern in the chiral metal phase. This panel shows the pattern of $I_{(ij)}^c$ at $\delta = 1/20$ for $U/t = 9$ on $L_y = 4$ cylinders, the width of each bond is proportional to the current magnitude, while the arrow indicates the current direction. Here we consider $N = 16 \times 4$ cylinders. The bond dimension of such calculation is set up to 12 000.

In addition, for these doping levels, we have found spatial charge modulations (see Appendix A 1), the number of peaks in the hole distribution function equals to the number of doped holes. This is inconsistent with a strongly paired state, where the number of peaks would be half the number of doped holes. Here, we also notice Ref. [73] fit $D(r)$ in to a power-law function with $\eta > 3.5$, which is consistent with our results and indicates the absence of divergent susceptibility, but it was claimed to be the evidence of superconducting state [73]. At larger doping $\delta \gtrsim 20\%$, where the SDWs are strongly suppressed [see Figs. 2(a4) and 2(b4)], $D(r)$ are further enhanced. If we fit $D(r)$ by a power-law function, as shown in the right panel of Fig. 9(b), the exponent $\eta \approx 3$ is relatively large, which suggests that the enhancement for doping below and above 20% are insignificant. This might be due to the stronger quantum fluctuations for $L_y = 3$.

On square lattice, the previous studies mainly focused on 1/8 doping [83–88] and reported the exponential decay of pair-pair correlations for $L_y = 4$ ladders [83–86] or 2D

[86], which was attributed to the competition between charge-density waves (or stripes) and superconductivity. Here, we have identified the doping induced commensurate SDWs at $\delta \approx 10\% \sim 20\%$, where the pair-pair correlations are strongly suppressed, implying the competition between SDWs and superconductivity on triangular lattice. We note that the existence of d-wave superconductivity is reported in the same triangular-lattice model for $L_y = 3$ ladders at $U/t = 10$ [68]. Our findings of the enhanced pairing at larger doping are consistent with hole pairing driven by spin super-exchange coupling, similar to the pairing mechanism proposed for square lattice case [2–4]. An additional observation that is consistent with the super-exchange scenario is that at intermediate coupling where the super-exchange $J \sim t^2/U$ exceeds that at strong coupling, the pair correlations are generally found to be stronger (compare the intermediate coupling correlators with the strong coupling correlators in the Appendix A 3).

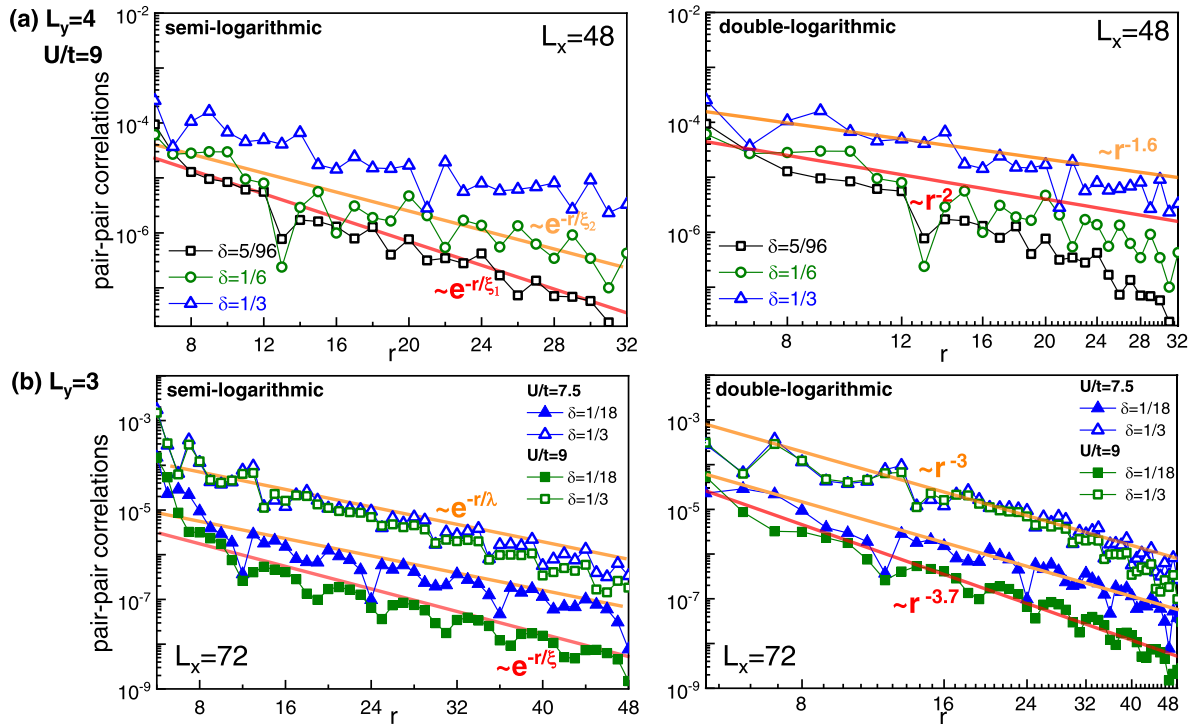


FIG. 9. The pair-pair correlations. Panels (a) and (b) show the pair-pair correlations in singlet channels for $U/t = 9$ on $L_y = 4$, $L_x = 48$ (a) and $L_y = 3$, $L_x = 72$ (b) cylinders. The left panels in each figure show the plots in semi-logarithmic scale, while the right panels are the plots in double-logarithmic scale. The bond dimension of such calculation is set up to 60 000.

TABLE I. Summary of results as a function of doping (light, moderate, and high as defined above) and coupling strength (intermediate and strong). The SDW phase has the same wave vector as the 120° magnetic order, but the wave vector in SDW' is at a potentially different (M) momentum point when K point is inaccessible. The anomalous chiral metal has short ranged spin correlations but long ranged spin chirality order. No clear Fermi surface is detected, unlike in the other regimes.

Doping	Intermediate coupling	Strong coupling
Light	Chiral order ($L_y = 3, 4$);	SDW;
$0 < \delta < 10\%$	Metallic ($L_y = 4$), Metallic vs local PDW ($L_y = 3$)	Metallic
Moderate	SDW';	SDW';
$10\% < \delta < 20\%$	Metallic	Metallic
High	no-SDW	no-SDW
$20\% < \delta$	enhanced singlet pairing	enhanced singlet pairing

Here, we should point out that at doping around $\delta = 1/3$, although we indeed find the pair-pair correlations are significantly enhanced than lower doping and they decay in a power-law fashion with the exponent $\eta < 2$ ($D(r) \sim 1/r^\eta$), our computations show that the single particle propagator also decays in a power-law fashion (see the Appendix A 3), which may indicate the existence of nodal points in the superconducting phase or the superconductivity is not robust. We therefore claim it as the enhanced pair-pair correlations in the phase diagram instead of the robust superconductivity. The absence of clear superconductivity in pure Hubbard model on triangular lattice is similar to the square-lattice case as reported in Refs. [84–86]. Meanwhile, we also find random sign oscillations in $D(r)$, indicating competing spatial symmetries or even more complicated nature, which we leave for future studies.

G. Particle-hole asymmetry

Based on the above measurement, we summarize our findings in Table I and set up the hole doped phase diagram as depicted in Fig. 10. Now we briefly discuss the particle-hole asymmetry with respect to electron and hole doping and leave a systematic study for future work. The particle-hole symmetry is absent on the nonbipartite triangular lattice. In contrast to the hole doped case, where light doping $\delta \sim 10\%$ does not change the spin background, even a small density of doped electrons have a dramatic effect on the spin background (see Appendix B). For example, at intermediate coupling even for doping as low as $\delta \sim 5\%$ the maxima of the spin-spin correlation function shift to wave vector \mathbf{M} (on $L_y = 3$ cylinders). The distinct spin backgrounds after doping characterize the asymmetric roles of the doped holes and electrons, suggesting even richer physics on triangular lattice compared with the particle-hole symmetric square-lattice case. We leave the systematic study of electron doping and particle-hole asymmetry to future work.

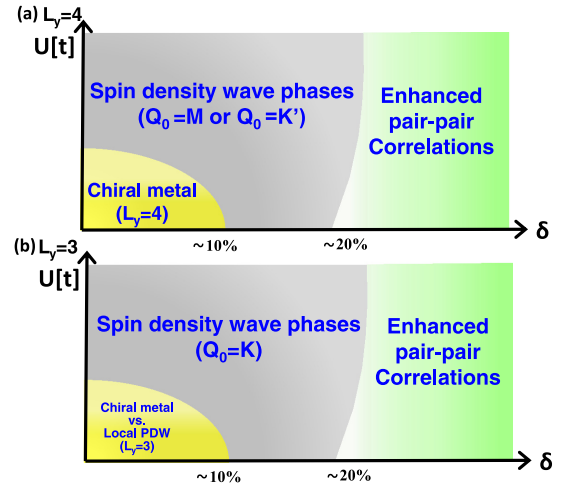


FIG. 10. . The schematic phase diagram of hole doped two distinct spin backgrounds for $U/t = 9$ and $U/t = 18$ as a function of hole doping concentrations δ . Here the chiral metallic phase is robust on $L_y = 4$ cylinders while it coexists with local PDW pattern (short-range PDW) on $L_y = 3$ cylinders

IV. CONCLUSIONS

Our study of the doped triangular lattice Hubbard model reveals that different Mott insulators obtained on changing the coupling strength U/t leads to significantly different physics at light hole doping. In the strong coupling limit, a Fermi liquid with well-defined hole pockets at the \mathbf{K}^\pm points is observed. In contrast at intermediate coupling, hole pockets do not exhibit well-defined quasiparticles. Moreover, long ranged spin chirality correlations along with short ranged spin-spin correlations are observed. These observations are consistent with spin-charge separation and spin liquid physics. However, at moderate doping and high doping, a SDW is established across the range of coupling strengths and competes with superconductivity, which is established on further doping. This phenomenology should be contrasted with the competition between the emergent charge density wave (CDW) and superconductivity on the square lattice. We summarize the main features of different phases versus doping concentration δ and coupling strength U/t in Table I and the schematic phase diagram in Fig. 10.

Our findings for the doped Mott insulators here open up the study of the distinct signatures of correlated electron physics on frustrated lattices, and the inherent electron-hole asymmetry in these problems. A promising platform to experimentally study these issues is the recently realized Moiré lattice TMD or twisted TMD bilayers [25,26], which should be well described by the triangular lattice Hubbard model, in which the coupling strength U/t is widely tunable through the twist angle, and the doping concentration is also continuously controllable. In a completely different context, in recent years, quantum simulations using the ultracold fermions in optical lattices has been significantly advanced by quantum gas microscopy [28–30], which provides another platform to explore the physics in the doped Hubbard models. The experimental architecture makes it possible to tune the lattice geometry, the charge doping and the coupling strength U/t , and therefore,

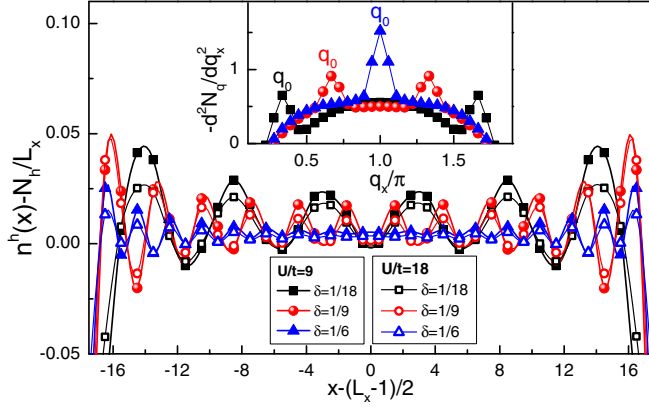


FIG. 11. The real-space hole density profile $n^h(x)$ for $U/t = 9$ and $U/t = 18$ at doping level $\delta = 1/18, 1/9, 1/6$ on $L_x = 36, L_y = 3$ cylinders. The inset shows the second order derivatives of the density structure factor N_q , where the peaks indicate the wave vectors of the charge modulations q_0 .

the whole phase diagram discovered in this paper could be directly probed.

Note added. A theoretical study [82] also found that a chiral metal naturally emerges on doping a Kalmeyer-Laughlin chiral spin liquid.

ACKNOWLEDGMENTS

We would like to thank Lesik Motrunich, Zheng-Yu Weng, Steven A. Kivelson, Max Metlitski, Bertrand Halperin, Zhi-Xun Shen, Ya-Hui Zhang, Ruben Verresen for valuable discussions. Z.Z. acknowledges the computational resources at Harvard, CSUN and KITS, the subsequent part of this work carried out at KITS was supported by the National Natural Science Foundation of China (Grant No. 12074375), the Fundamental Research Funds for the Central Universities, the start-up funding of UCAS (Grant No. 118900M026) and the Strategic Priority Research Program of CAS (Grant No. XDB33000000). DNS was supported by the U.S. Department of Energy, Office of Basic Energy Sciences under Grant No. DE-FG02-06ER46305 for performing larger scale DMRG simulations, A.V. was supported by a Simons Investigator award.

APPENDIX A: ADDITIONAL RESULTS FOR HOLE DOPING

1. Charge Modulations

We first present the results of the real-space charge density distribution of the doped holes. The doped holes distribute uniformly in each rung of cylinder due to the periodical

boundary conditions along \mathbf{e}_y , we thus focus on the hole distribution along \mathbf{e}_x and define $n^h(x) \equiv \sum_{y=1}^{L_y} n^h(x, y)$, where $n^h(x, y) \equiv 1 - n(x, y)$ denotes the hole density on the site with coordinate (x, y) . As shown in Fig. 11 for $U/t = 9$ and $U/t = 18$, the doped holes exhibit strongly spatial modulations at $\delta \lesssim 20\%$ for both cases, while their amplitude decrease with the increase of hole concentration. The wave vectors of the charge modulations q_0 can be determined by the singularity/kinks in the structure factors N_q , as illustrated in the second order derivative of N_q in the inset of Fig. 11. Moreover, the number of peaks in $n^h(x)$ equals to the number of doped holes, implying the absence of strongly pairing state.

2. Charge current pattern for $L_y = 3$ cylinders

In the main text, we have shown the bond charge current pattern for the chiral metallic phase on $L_y = 4$ cylinders. Figure 12 shows the bond charge current pattern on $L_y = 3$ cylinders with $U/t = 9$, the width of each bond is proportional to the current magnitude and the arrow indicates the current direction, the bond current pattern exhibits the translational symmetry breaking in the bulk along the horizontal direction, though we also notice the existence of domains in the pattern. Meanwhile, the time-reversal invariant spin current $I_{ij}^s \equiv -i\langle S_i^+ S_j^- - S_i^- S_j^+ \rangle$ is vanishingly small in the same phase, consistent with the existence of the spin chirality order for chiral metal.

3. Various real-space correlators

To further confirm the dominant physics in each phase, we compute various correlation functions in the real space and put them into the same figure to compare, including: (i) the spin-spin correlation: $\langle S_i^z S_{i+r}^z \rangle$; (ii) the charge density-density correlation: $\langle n_i n_{i+r} \rangle - \langle n_i \rangle \langle n_{i+r} \rangle$; (iii) the single particle propagator: $\sum_{\sigma} \langle c_{i\sigma}^\dagger c_{i+r,\sigma} \rangle$; and (iv) the chiral-chiral correlations $|\langle C_{\Delta_i} C_{\Delta_{i+r}} \rangle|$, as shown in Fig. 13. Figures 13(a)–13(c) and 13(d)–13(f) show $L_y = 4, L_x = 48$ cylinders and $L_y = 3, L_x = 72$ cylinders at three typical dopings, respectively.

4. Pair-pair correlations

We next examine the pair-pair correlations $D(r)$ at hole doping side. In the main text, we have shown the results on longer cylinders with size $N = 72 \times 3$ and $N = 48 \times 4$. In the Appendix, we show the bond-dimension dependence of the pair-pair correlations.

At light doping, the pairing correlators appear to decay exponentially and there is no systematic change of correlators on increasing bond dimension on small clusters with $N = 36 \times 3$, as shown in Fig. 14 for $L_y = 3$ cylinders and Fig. 15 for $L_y = 4$ cylinders. If we fit $D(r)$ with a power law function

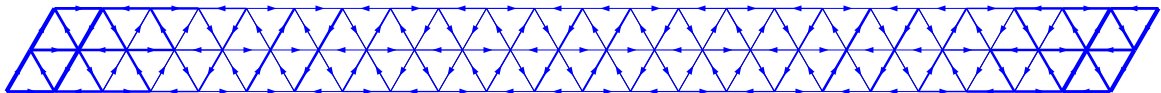


FIG. 12. The charge current pattern in the chiral metal phase. This panel shows the pattern of I_{ij}^c at $\delta = 1/18$ for $U/t = 9$ on $L_y = 3$ cylinders, the width of each bond is proportional to the current magnitude, while the arrow indicates the current direction. Here we consider $N = 24 \times 3$ cylinders. The bond dimension of such calculation is set up to 12 000.

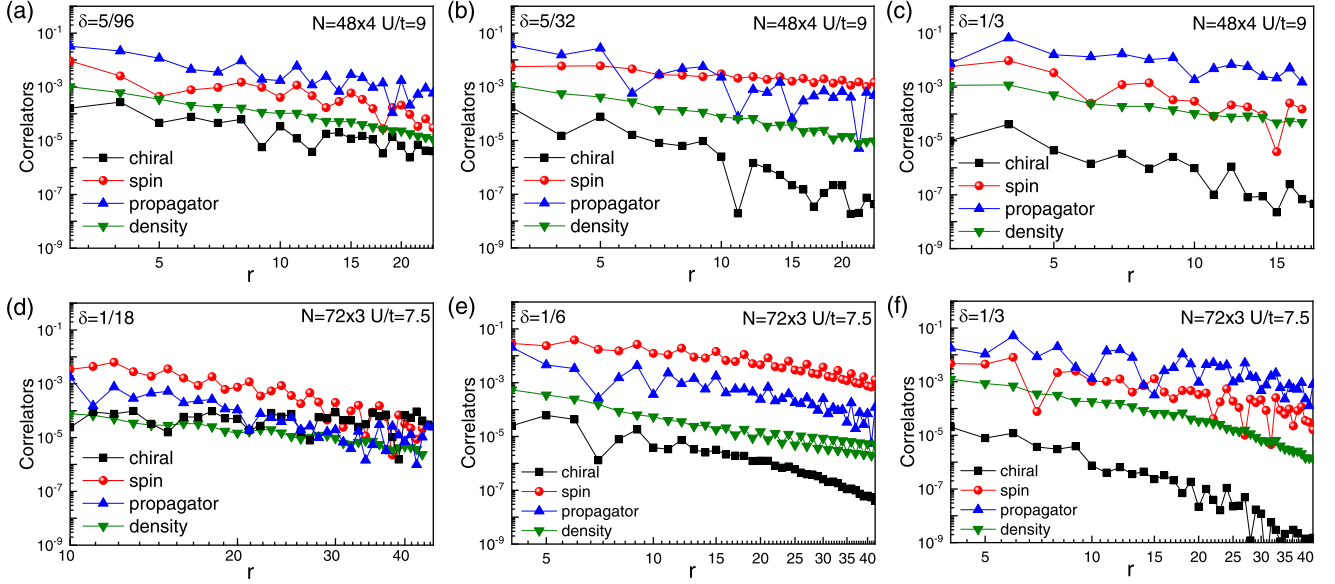


FIG. 13. Real-space correlators: chiral-chiral correlations, spin-spin correlations, charge density-density correlations, single particle propagators. Panels [(a)–(c)] and panels [(d)–(f)] show different correlators for $U/t = 9$ on $L_y = 4$ and for $U/t = 7.5$ on $L_y = 3$ cylinders, respectively. From left to right in each row, we consider three typical hole doping concentrations: $\delta = 1/18$ [(a),(d)], $\delta = 1/6$ [(b),(e)], and $\delta = 1/3$ [(c),(f)].

$D(r) \sim r^{-\alpha}$ as best we can, the resulting exponent is relatively large. For instance, $\alpha \gtrsim 4$ for $\delta = 1/18$ when $L_y = 3$ [see Fig. 14(b)] and $\alpha \gtrsim 3$ for $\delta = 1/20$ when $L_y = 4$ [see Fig. 15(b)]. Furthermore, while this behavior is potentially also consistent with a power law with large exponent, we note that the smallness of correlators both in absolute magnitude and rapid decay rate does not point to a superconducting ground state at small and medium doping. In addition, for these doping levels, we have found spatial charge modulations in Fig. 11, the number of peaks in the hole distribution function equals to the number of doped holes. This is inconsistent with a strongly paired state, where the number of peaks would be half the number of doped holes.

APPENDIX B: ELECTRON DOPING

In the main text, we mainly focus on the hole doped side, in this section, we very briefly compare with electron doping side. For the electron doping, we choose $U/t = 9$ and

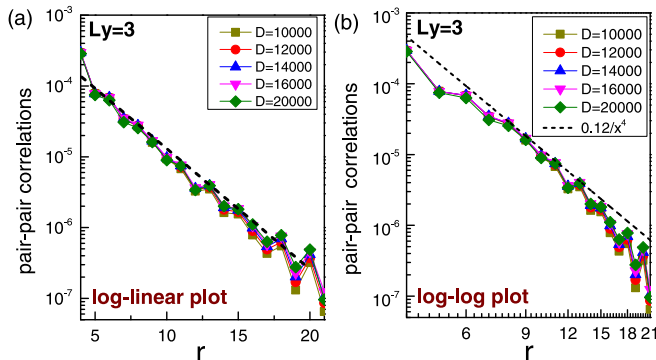


FIG. 14. The pair-pair correlations for $N = 36 \times 3$ cylinders at doping $\delta = 1/18$. Panel (a) shows the plots in semilogarithmic scale, while panel (b) shows the same data but in double-logarithmic scale.

$U/t = 18$ for comparative study on $L_y = 3$ cylinders at doping $\delta > 5\%$. Here, we should point out that the comprehensive study of electron doping lies outside the scope of the present work, which we will leave for future systematical investigations.

We examine the spin channel by measuring the static spin structure factor $S_q(\mathbf{Q}) = \frac{1}{N} \sum_{i,j} \langle S_i^z S_j^z \rangle e^{i\mathbf{Q} \cdot (\mathbf{r}_i - \mathbf{r}_j)}$. Figures 16(a)–16(d) and 16(e)–16(h) show the contour plot of S_q against electron doping with $U/t = 9$ and $U/t = 18$, respectively. For the electron doping with $U/t = 9$, S_q exhibits peaks at commensurate momentum $\mathbf{q} = \mathbf{M}$ up to around $\delta = 1/6$ [see Figs. 16(a)–16(c)], indicating the commensurate SDWs. For the electron doped 120° Néel ordered spin background with $U/t = 18$ [see Figs. 16(e)–16(g)], S_q exhibits splitting peaks around $\mathbf{q} = \mathbf{M}$, suggesting incommensurate SDWs. At larger doping $\delta > 20\%$, the spin backgrounds are

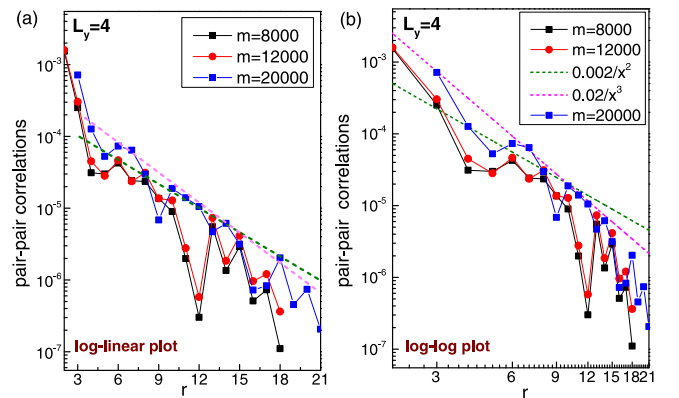


FIG. 15. The pair-pair correlations for $N = 30 \times 4$ cylinders at doping $\delta = 1/20$. Panel (a) shows the plots in semilogarithmic scale, while panel (b) shows the same data but in double-logarithmic scale.

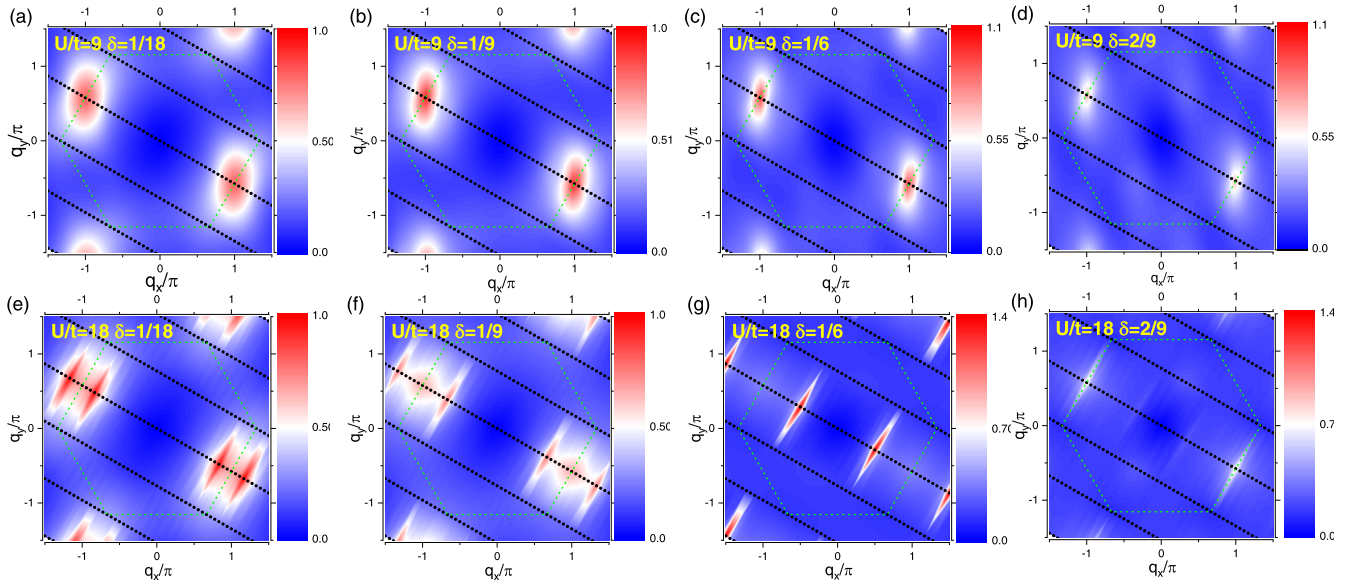


FIG. 16. The contour plot of spin structure factor S_q for $U/t = 9$ [(a)–(d)] and $U/t = 18$ [(e)–(h)] with different electron doping concentrations δ . From left to right in each row, the concentrations of the doped electrons are $\delta = 1/18$ [(a),(e)], $\delta = 1/9$ [(b),(f)], $\delta = 1/6$ [(c),(g)], $\delta = 2/9$ [(d),(h)]. The black dots represent the momentum points we can access in the Brillouin zone (dashed line) of $N = 36 \times 3$ cylinders.

indistinguishable for $U/t = 9$ and $U/t = 18$ [see Figs. 16(d) and 16(h)], the spin correlations become short ranged for both coupling strength. The different responses of the spin

backgrounds against doping can be served as an evidence of the asymmetry with respect to the electron and hole doping on triangular lattice.

- [1] P. W. Anderson, *Science* **235**, 1196 (1987); *The Theory of Superconductivity in the High-Tc Cuprates* (Princeton University Press, Princeton, NJ, 1997).
- [2] E. Dagotto, Correlated electrons in high-temperature superconductors, *Rev. Mod. Phys.* **66**, 763 (1994) and references therein.
- [3] P. A. Lee, N. Nagaosa, and X. G. Wen, Doping a Mott insulator: Physics of high-temperature superconductivity, *Rev. Mod. Phys.* **78**, 17 (2006) and references therein.
- [4] B. Keimer, S. A. Kivelson, M. R. Norman, S. Uchida, and J. Zaanen, From quantum matter to high-temperature superconductivity in copper oxides, *Nature (London)* **518**, 179 (2015) and references therein.
- [5] L. Balents, Spin liquids in frustrated magnets, *Nature (London)* **464**, 199 (2010); L. Savary and L. Balents, Quantum spin liquids: A review, *Rep. Prog. Phys.* **80**, 016502 (2017).
- [6] Y. Zhou, K. Kanoda, and T.-K. Ng, Quantum spin liquid states, *Rev. Mod. Phys.* **89**, 025003 (2017).
- [7] Y. Shimizu, K. Miyagawa, K. Kanoda, M. Maesato, and G. Saito, Spin Liquid State in an Organic Mott Insulator with a Triangular Lattice, *Phys. Rev. Lett.* **91**, 107001 (2003).
- [8] T. Itou, A. Oyamada, S. Maegawa, M. Tamura, and R. Kato, Spin-liquid state in an organic spin-1/2 system on a triangular lattice, $\text{EtMe}_3\text{Sb}[\text{Pd}(\text{dmit})_2]_2$, *J. Phys.: Condens. Matter* **19**, 145247 (2007); Quantum spin liquid in the spin-1/2 triangular antiferromagnet $\text{EtMe}_3\text{Sb}[\text{Pd}(\text{dmit})_2]_2$, *Phys. Rev. B* **77**, 104413 (2008).
- [9] T. Itou, A. Oyamada, S. Maegawa, and R. Kato, Instability of a quantum spin liquid in an organic triangular-lattice antiferromagnet, *Nat. Phys.* **6**, 673 (2010).
- [10] M. Yamashita, N. Nakata, Y. Senshu, M. Nagata, H. M. Yamamoto, R. Kato, T. Shibauchi, Y. Matsuda, Highly mobile gapless excitations in a two-dimensional candidate quantum spin liquid, *Science* **328**, 1246 (2010).
- [11] S. Yamashita, T. Yamamoto, Y. Nakazawa, M. Tamura, and R. Kato, Gapless spin liquid of an organic triangular compound evidenced by thermodynamic measurements, *Nat. Commun.* **2**, 275 (2011).
- [12] T. Isono, H. Kamo, A. Ueda, K. Takahashi, M. Kimata, H. Tajima, S. Tsuchiya, T. Terashima, S. Uji, and H. Mori, Gapless Quantum Spin Liquid in an Organic Spin-1/2 Triangular-Lattice, $\kappa\text{-H}_3(\text{Cat-EDT-TTF})_2$, *Phys. Rev. Lett.* **112**, 177201 (2014).
- [13] H. D. Zhou, E. S. Choi, G. Li, L. Balicas, C. R. Wiebe, Y. Qiu, J. R. D. Copley, and J. S. Gardner, Spin Liquid State in the $S = 1/2$ Triangular Lattice $\text{Ba}_3\text{CuSb}_2\text{O}_9$, *Phys. Rev. Lett.* **106**, 147204 (2011).
- [14] K. A. Ross, L. Savary, B. D. Gaulin, and L. Balents, Quantum Excitations in Quantum Spin Ice, *Phys. Rev. X* **1**, 021002 (2011).
- [15] S. A. Zvyagin, D. Kamenskyi, M. Ozerov, J. Wosnitzer, M. Ikeda, T. Fujita, M. Hagiwara, A. I. Smirnov, T. A. Soldatov, A. Ya. Shapiro, J. Krzystek, R. Hu, H. Ryu, C. Petrovic, and M. E. Zhitomirsky, Direct Determination of Exchange Parameters in Cs_2CuBr_4 and Cs_2CuCl_4 : High-Field Electron-Spin-Resonance Studies, *Phys. Rev. Lett.* **112**, 077206 (2014).
- [16] S. A. Zvyagin, D. Graf, T. Sakurai, S. Kimura, H. Nojiri, J. Wosnitzer, H. Ohta, T. Ono, and H. Tanaka, Pressure-tuning the quantum spin Hamiltonian of the triangular

- lattice antiferromagnet Cs_2CuCl_4 , *Nat. Commun.* **10**, 1064 (2019).
- [17] G. Koutoulakis, T. Zhou, Y. Kamiya, J. D. Thompson, H. D. Zhou, C. D. Batista, and S. E. Brown, Quantum phase diagram of the $S = 1/2$ triangular-lattice antiferromagnet $\text{Ba}_3\text{CoSb}_2\text{O}_9$, *Phys. Rev. B* **91**, 024410 (2015).
- [18] Y. Li, H. Liao, Z. Zhang, S. Li, F. Jin, L. Ling, L. Zhang, Y. Zou, L. Pi, Z. Yang, J. Wang, Z. Wu, and Q. Zhang, Gapless quantum spin liquid ground state in the two-dimensional spin- $1/2$ triangular antiferromagnet YbMgGaO_4 , *Sci. Rep.* **5**, 16419 (2015).
- [19] M. G. Kim, B. Winn, S. Chi, A. T. Savici, J. A. Rodriguez-Rivera, W. C. Chen, X. Xu, Y. Li, J. W. Kim, S.-W. Cheong, and V. Kiryukhin, Spin-liquid-like state in pure and Mn-doped TbInO_3 with a nearly triangular lattice, *Phys. Rev. B* **100**, 024405 (2019).
- [20] M. Bordelon, E. Kenney, T. Hogan, L. Posthuma, M. Kavand, Y. Lyu, M. Sherwin, C. Brown, M. J. Graf, L. Balents, S. D. Wilson, Field-tunable quantum disordered ground state in the triangular-lattice antiferromagnet NaYbO_2 , *Nat. Phys.* **15**, 1058 (2019).
- [21] L. Ding, P. Manuel, S. Bachus, F. Grüber, P. Gegenwart, J. Singleton, R. D. Johnson, H. C. Walker, D. T. Adroja, A. D. Hillier, A. A. Tsirlin, Gapless spin-liquid state in the structurally disorder-free triangular antiferromagnet NaYbO_2 , *Phys. Rev. B* **100**, 144432 (2019).
- [22] F. Wu, T. Lovorn, E. Tutuc, and A. H. MacDonald, Hubbard Model Physics in Transition Metal Dichalcogenide Moiré Bands, *Phys. Rev. Lett.* **121**, 026402 (2018).
- [23] K. T. Law and P. A. Lee, 1T-TaS₂ as a quantum spin liquid, *Proc. Natl. Acad. Sci. USA* **114**, 6996 (2017); W.-Y. He, X. Y. Xu, G. Chen, K. T. Law, and P. A. Lee, Spinon Fermi Surface in a Cluster Mott Insulator Model on a Triangular Lattice and Possible Application to 1T-TaS₂, *Phys. Rev. Lett.* **121**, 046401 (2018).
- [24] F. Wu, T. Lovorn, E. Tutuc, I. Martin, and A. H. MacDonald, Topological Insulators in Twisted Transition Metal Dichalcogenide Homobilayers, *Phys. Rev. Lett.* **122**, 086402 (2019).
- [25] Y. Tang, L. Li, T. Li, Y. Xu, S. Liu, K. Barmak, K. Watanabe, T. Taniguchi, A. H. MacDonald, J. Shan, and K. F. Mak, Simulation of Hubbard model physics in WSe_2/WS_2 moiré superlattices, *Nature* **579**, 353 (2020).
- [26] L. Wang, E.-M. Shih, A. Ghiotto, L. Xian, D. A. Rhodes, C. Tan, M. Claassen, D. M. Kennes, Y. Bai, B. Kim *et al.*, Correlated electronic phases in twisted bilayer transition metal dichalcogenides, *Nat. Mater.* **19**, 861 (2020).
- [27] J. Yang, L. Liu, J. Mongkolkeha, and P. Schauss, Site-Resolved Imaging of Ultracold Fermions in a Triangular-Lattice Quantum Gas Microscope, *PRX Quantum* **2**, 020344 (2021).
- [28] W. S. Bakr, J. I. Gillen, A. Peng, S. Foelling, and M. Greiner, A quantum gas microscope for detecting single atoms in a Hubbard-regime optical lattice, *Nature (London)* **462**, 74 (2009); M. F. Parsons, A. Mazurenko, C. S. Chiu, Geoffrey Ji, D. Greif, and M. Greiner, Site-resolved measurement of the spin-correlation function in the Fermi-Hubbard model, *Science* **353**, 1253 (2016).
- [29] J. F. Sherson, C. Weitenberg, M. Endres, M. Cheneau, I. Bloch, and S. Kuhr, Single-atom-resolved fluorescence imaging of an atomic Mott insulator, *Nature (London)* **467**, 68 (2010).
- [30] L. W. Cheuk, M. A. Nichols, K. R. Lawrence, M. Okan, H. Zhang, E. Khatami, N. Trivedi, T. Paiva, M. Rigol, and M. W. Zwierlei, Observation of spatial charge and spin correlations in the 2D Fermi-Hubbard model, *Science* **353**, 1260 (2016).
- [31] H. R. Krishnamurthy, C. Jayaprakash, S. Sarker, and W. Wenzel, Mott-Hubbard metal-insulator transition in nonbipartite lattices, *Phys. Rev. Lett.* **64**, 950 (1990); C. Jayaprakash, H. R. Krishnamurthy, S. Sarker, and W. Wenzel, Metal-insulator transition in the Hubbard model on a triangular lattice, *Europhys. Lett.* **15**, 625 (1991).
- [32] M. Capone, L. Capriotti, F. Becca, and S. Caprara, Mott metal-insulator transition in the half-filled Hubbard model on the triangular lattice, *Phys. Rev. B* **63**, 085104 (2001).
- [33] S. Sachdev, Kagome- and triangular-lattice Heisenberg antiferromagnets: Ordering from quantum fluctuations and quantum-disordered ground states with unconfined bosonic spinons, *Phys. Rev. B* **45**, 12377 (1992).
- [34] F. Wang and A. Vishwanath, Spin-liquid states on the triangular and Kagome lattices: A projective-symmetry-group analysis of Schwinger boson states, *Phys. Rev. B* **74**, 174423 (2006).
- [35] X.-Y. Song, C. Wang, A. Vishwanath, and Yin-Chen He, Unifying description of competing orders in two-dimensional quantum magnets, *Nat. Commun.* **10**, 4254 (2019).
- [36] D. A. Huse and V. Elser, Simple Variational Wave Functions for Two-Dimensional Heisenberg Spin- $1/2$ Antiferromagnets, *Phys. Rev. Lett.* **60**, 2531 (1988).
- [37] O. I. Motrunich, Variational study of triangular lattice spin- $1/2$ model with ring exchanges and spin liquid state in $\kappa\text{-(ET)}_2\text{Cu}_2(\text{CN})_3$, *Phys. Rev. B* **72**, 045105 (2005).
- [38] T. Koretsune, Y. Motome, and A. Furusaki, Exact diagonalization study of Mott transition in the Hubbard model on an anisotropic triangular lattice, *J. Phys. Soc. Jpn.* **76**, 074719 (2007).
- [39] P. Sahebsara and D. Sénéchal, Hubbard Model on the Triangular Lattice: Spiral Order and Spin Liquid, *Phys. Rev. Lett.* **100**, 136402 (2008).
- [40] R. T. Clay, H. Li, and S. Mazumdar, Absence of Superconductivity in the Half-Filled Band Hubbard Model on the Anisotropic Triangular Lattice, *Phys. Rev. Lett.* **101**, 166403 (2008).
- [41] T. Watanabe, H. Yokoyama, Y. Tanaka, and J. Inoue, Predominant magnetic states in the Hubbard model on anisotropic triangular lattices, *Phys. Rev. B* **77**, 214505 (2008).
- [42] D. Galanakis, T. D. Stanescu, and P. Phillips, Mott transition on a triangular lattice, *Phys. Rev. B* **79**, 115116 (2009).
- [43] T. Yoshioka, A. Koga, and N. Kawakami, Quantum Phase Transitions in the Hubbard Model on a Triangular Lattice, *Phys. Rev. Lett.* **103**, 036401 (2009).
- [44] H. Y. Yang, A. M. Läuchli, F. Mila, and K. P. Schmidt, Effective Spin Model for the Spin-Liquid Phase of the Hubbard Model on the Triangular Lattice, *Phys. Rev. Lett.* **105**, 267204 (2010).
- [45] J. Kokalj and R. H. McKenzie, Thermodynamics of a Bad Metal–Mott Insulator Transition in the Presence of Frustration, *Phys. Rev. Lett.* **110**, 206402 (2013).
- [46] A. Yamada, Magnetic properties and Mott transition in the Hubbard model on the anisotropic triangular lattice, *Phys. Rev. B* **89**, 195108 (2014).

- [47] G. Li, A. E. Antipov, A. N. Rubtsov, S. Kirchner, and W. Hanke, Competing phases of the Hubbard model on a triangular lattice: Insights from the entropy, *Phys. Rev. B* **89**, 161118(R) (2014).
- [48] L. F. Tocchio, H. Feldner, F. Becca, R. Valentí, and C. Gros, Spin-liquid versus spiral-order phases in the anisotropic triangular lattice, *Phys. Rev. B* **87**, 035143 (2013); L. F. Tocchio, C. Gros, R. Valentí, and F. Becca, One-dimensional spin liquid, collinear, and spiral phases from uncoupled chains to the triangular lattice, *Phys. Rev. B* **89**, 235107 (2014).
- [49] M. Laubach, R. Thomale, C. Platt, W. Hanke, and G. Li, Phase diagram of the Hubbard model on the anisotropic triangular lattice, *Phys. Rev. B* **91**, 245125 (2015).
- [50] R. V. Mishmash, I. González, R. G. Melko, O. I. Motrunich, and M. P. A. Fisher, Continuous Mott transition between a metal and a quantum spin liquid, *Phys. Rev. B* **91**, 235140 (2015).
- [51] Y. Iqbal, W.-J. Hu, R. Thomale, D. Poilblanc, and F. Becca, Spin liquid nature in the Heisenberg J_1 - J_2 triangular antiferromagnet, *Phys. Rev. B* **93**, 144411 (2016).
- [52] T. Shirakawa, T. Tohyama, J. Kokalj, S. Sota, and S. Yunoki, Ground-state phase diagram of the triangular lattice Hubbard model by the density-matrix renormalization group method, *Phys. Rev. B* **96**, 205130 (2017).
- [53] A. Szasz, J. Motruk, M. P. Zaletel, J. E. Moore, Chiral Spin Liquid Phase of the Triangular Lattice Hubbard Model: A Density Matrix Renormalization Group Study, *Phys. Rev. X* **10**, 021042 (2020).
- [54] A. Szasz and J. Motruk, Phase diagram of the anisotropic triangular lattice Hubbard model, *Phys. Rev. B* **103**, 235132 (2021).
- [55] B.-B. Chen, Z. Chen, S.-S. Gong, D. N. Sheng, W. Li, and A. Weichselbaum, Quantum spin liquid with emergent chiral order in the triangular-lattice Hubbard model, [arXiv:2102.05560](https://arxiv.org/abs/2102.05560).
- [56] A. Wietek, R. Rossi, F. Šimkovic IV, M. Klett, P. Hanmann, M. Ferrero, E. M. Stoudenmire, T. Schäfer, and A. Georges, Mott Insulating States with Competing Orders in the Triangular Lattice Hubbard Model, *Phys. Rev. X* **11**, 041013 (2021).
- [57] S. Hu, W. Zhu, S. Eggert, and Y.-C. He, Dirac Spin Liquid on the Spin-1/2 Triangular Heisenberg Antiferromagnet, *Phys. Rev. Lett.* **123**, 207203 (2019).
- [58] S. A. Chen, Q. Chen, and Z. Zhu, Proposal for asymmetric photoemission and tunneling spectroscopies in Fermi-Hubbard model on triangular optical lattices, [arXiv:2202.05855](https://arxiv.org/abs/2202.05855).
- [59] G. Baskaran, Electronic Model for CoO_2 Layer Based Systems: Chiral Resonating Valence Bond Metal and Superconductivity, *Phys. Rev. Lett.* **91**, 097003 (2003).
- [60] B. Kumar and B. S. Shastry, Superconductivity in CoO_2 layers and the resonating valence bond mean-field theory of the triangular lattice t - J model, *Phys. Rev. B* **68**, 104508 (2003).
- [61] Q.-H. Wang, D.-H. Lee, P. A. Lee, Doped t - J model on a triangular lattice: Possible application to $\text{Na}_x\text{CoO}_2 \cdot y\text{H}_2\text{O}$ and $\text{Na}_{1-x}\text{TiO}_2$, *Phys. Rev. B* **69**, 092504 (2004).
- [62] O. I. Motrunich and P. A. Lee, Study of the triangular lattice tV model near $x = 1/3$, *Phys. Rev. B* **70**, 024514 (2004).
- [63] S. Raghu, S. A. Kivelson, and D. J. Scalapino, Superconductivity in the repulsive Hubbard model: An asymptotically exact weak-coupling solution, *Phys. Rev. B* **81**, 224505 (2010).
- [64] T. Watanabe, H. Yokoyama, Y. Tanaka, J.-i. Inoue, and M. Ogata, Variational Monte Carlo studies of pairing symmetry for the t - J model on a triangular lattice, *J. Phys. Soc. Jpn.* **73**, 3404 (2004).
- [65] K. S. Chen, Z. Y. Meng, U. Yu, S. Yang, M. Jarrell, and J. Moreno, Unconventional superconductivity on the triangular lattice Hubbard model, *Phys. Rev. B* **88**, 041103(R) (2013).
- [66] B. Ye, A. Mesaros, and Y. Ran, Ferromagnetism and d+id superconductivity in 1/2 doped correlated systems on triangular lattice, [arXiv:1604.08615](https://arxiv.org/abs/1604.08615).
- [67] N. Gomes, W. W. De Silva, T. Dutta, R. T. Clay, and S. Mazumdar, Coulomb-enhanced superconducting pair correlations and paired-electron liquid in the frustrated quarter-filled band, *Phys. Rev. B* **93**, 165110 (2016); W. W. De Silva, N. Gomes, S. Mazumdar, and R. T. Clay, Coulomb enhancement of superconducting pair-pair correlations in a 3/4-filled model for κ -(BEDT-TTF) $_2\text{X}$, *Phys. Rev. B* **93**, 205111 (2016).
- [68] J. Venderley, E. A. Kim, Density matrix renormalization group study of superconductivity in the triangular lattice Hubbard model, *Phys. Rev. B* **100**, 060506(R) (2019).
- [69] Y. Gannot, Y.-F. Jiang, and S. A. Kivelson, Hubbard ladders at small U revisited, *Phys. Rev. B* **102**, 115136 (2020).
- [70] S. R. White, Density matrix formulation for quantum renormalization groups, *Phys. Rev. Lett.* **69**, 2863 (1992); S. R. White, Density-matrix algorithms for quantum renormalization groups, *Phys. Rev. B* **48**, 10345 (1993).
- [71] S. Östlund and S. Rommer, Thermodynamic Limit of Density Matrix Renormalization, *Phys. Rev. Lett.* **75**, 3537 (1995).
- [72] I. Affleck, Quantum spin chains and the Haldane gap, *J. Phys.: Condens. Matter* **1**, 3047 (1989).
- [73] C. Peng, Y.-F. Jiang, Y. Wang, and H.-C. Jiang, Gapless spin liquid and pair density wave of the Hubbard model on three-leg triangular cylinders, *New J. Phys.* **23**, 123004 (2021).
- [74] W. Kadow, L. Vanderstraeten, and M. Knap, Hole spectral function of a chiral spin liquid in the triangular lattice Hubbard model, [arXiv:2202.03458](https://arxiv.org/abs/2202.03458).
- [75] Z. Zhu, D. N. Sheng, and Z.-Y. Weng, Intrinsic translational symmetry breaking in a doped Mott insulator, *Phys. Rev. B* **98**, 035129 (2018).
- [76] W. Zheng, Z. Zhu, D. N. Sheng, and Z.-Y. Weng, Hidden spin current in doped Mott antiferromagnets, *Phys. Rev. B* **98**, 165102 (2018).
- [77] Z. Zhu, D. N. Sheng, Z.-Y. Weng, Pairing versus phase coherence of doped holes in distinct quantum spin backgrounds, *Phys. Rev. B* **97**, 115144 (2018).
- [78] Z. Zhu and Z.-Y. Weng, Quasiparticle collapsing in an anisotropic t - J ladder, *Phys. Rev. B* **92**, 235156 (2015).
- [79] R.-Y. Sun, Z. Zhu, and Z.-Y. Weng, Localization in a t - J -Type Model with Translational Symmetry, *Phys. Rev. Lett.* **123**, 016601 (2019).
- [80] Z. Zhu, Q.-R. Wang, D. N. Sheng, Z.-Y. Weng, Exact sign structure of the t - J chain and the single hole ground state, *Nucl. Phys. B* **903**, 51 (2016).
- [81] V. Kalmeyer and R. B. Laughlin, Equivalence of the resonating-valence-bond and fractional quantum Hall states, *Phys. Rev. Lett.* **59**, 2095 (1987).
- [82] X.-Y. Song, A. Vishwanath, and Y.-H. Zhang, Doping the chiral spin liquid: Topological superconductor or chiral metal? *Phys. Rev. B* **103**, 165138 (2021).

- [83] G. Ehlers, S. R. White, and R. M. Noack, Hybrid-space density matrix renormalization group study of the doped two-dimensional Hubbard model, [Phys. Rev. B **95**, 125125 \(2017\)](#).
- [84] H.-C. Jiang, T. P. Devereaux, Superconductivity in the doped Hubbard model and its interplay with next-nearest hopping t' , [Science **365**, 1424 \(2019\)](#).
- [85] C.-M. Chung, M. Qin, S. Zhang, U. Schollwöck, and S. R. White, Plaquette versus ordinary d -wave pairing in the t' -Hubbard model on a width-4 cylinder, [Phys. Rev. B **102**, 041106\(R\) \(2020\)](#).
- [86] M. Qin, C.-M. Chung, H. Shi, E. Vitali, C. Hubig, U. Schollwöck, S. R. White, S. Zhang, Absence of Superconductivity in the Pure Two-Dimensional Hubbard Model, [Phys. Rev. X **10**, 031016 \(2020\)](#).
- [87] M. Dolfi, B. Bauer, S. Keller, and M. Troyer, Pair correlations in doped Hubbard ladders, [Phys. Rev. B **92**, 195139 \(2015\)](#).
- [88] R. M. Noack, N. Bulut, D. J. Scalapino, and M. G. Zacher, Enhanced $d_{x^2} - d_{y^2}$ pairing correlations in the two-leg Hubbard ladder, [Phys. Rev. B **56**, 7162 \(1997\)](#).